The impacts of the mitochondrial myopathy-associated G58R mutation on the dynamic structural properties of CHCHD10

Hakan Alici, Vladimir N. Uversky, David E. Kang, Junga Alexa Woo & Orkid Coskuner-Weber

⊞ View supplementary material ☐

▦ Published online: 22 Jun 2023.

☐ Submit your article to this journal ☐

▥ Article views: 125

☐ View related articles ☐

CrossMark View Crossmark data ☐

Taylor & Francis
Taylor & Francis Group

Check for updates

The impacts of the mitochondrial myopathy-associated G58R mutation on the dynamic structural properties of CHCHD10

Hakan Alici[a], Vladimir N. Uversky[b] [ID], David E. Kang[c,d], Junga Alexa Woo[c] and Orkid Coskuner-Weber[e]

[a]Faculty of Sciences, Department of Physics, Zonguldak Bulent Ecevit University, Zonguldak, Turkey; [b]Department of Molecular Medicine and USF Health Byrd Alzheimer's Research Institute, Morsani College of Medicine, University of South Florida, Tampa, FL, USA; [c]School of Medicine, Department of Pathology, Case Western Reserve University, Cleveland, USA; [d]Louis Stokes Cleveland VA Medical Center, Cleveland, USA; [e]Molecular Biotechnology, Turkish-German University, Istanbul, Turkey

Communicated by Ramaswamy H. Sarma

ABSTRACT

The mitochondria are responsible for producing energy within the cell, and in mitochondrial myopathy, there is a defect in the energy production process. The CHCHD10 gene codes for a protein called coiled-coil-helix-coiled-coil-helix domain-containing protein 10 (CHCHD10), which is found in the mitochondria and is involved in the regulation of mitochondrial function. G58R mutation has been shown to disrupt the normal function of CHCHD10, leading to mitochondrial dysfunction and ultimately to the development of mitochondrial myopathy. The structures of G58R mutant CHCHD10 and how G58R mutation impacts the wild-type CHCHD10 protein at the monomeric level are unknown. To address this problem, we conducted homology modeling, multiple run molecular dynamics simulations and bioinformatics calculations. We represent herein the structural ensemble properties of the G58R mutant CHCHD10 (CHCHD10^{G58R}) in aqueous solution. Moreover, we describe the impacts of G58R mutation on the structural ensembles of wild-type CHCHD10 (CHCHD10^{WT}) in aqueous solution. The dynamics properties as well as structural properties of CHCHD10^{WT} are impacted by the mitochondrial myopathy-related G58R mutation. Specifically, the secondary and tertiary structure properties, root mean square fluctuations, Ramachandran diagrams and results from principal component analysis demonstrate that the CHCHD10^{WT} and CHCHD10^{G58R} proteins possess different structural ensemble characteristics and describe the impacts of G58R mutation on CHCHD10^{WT}. These findings may be helpful for designing new treatments for mitochondrial myopathy.
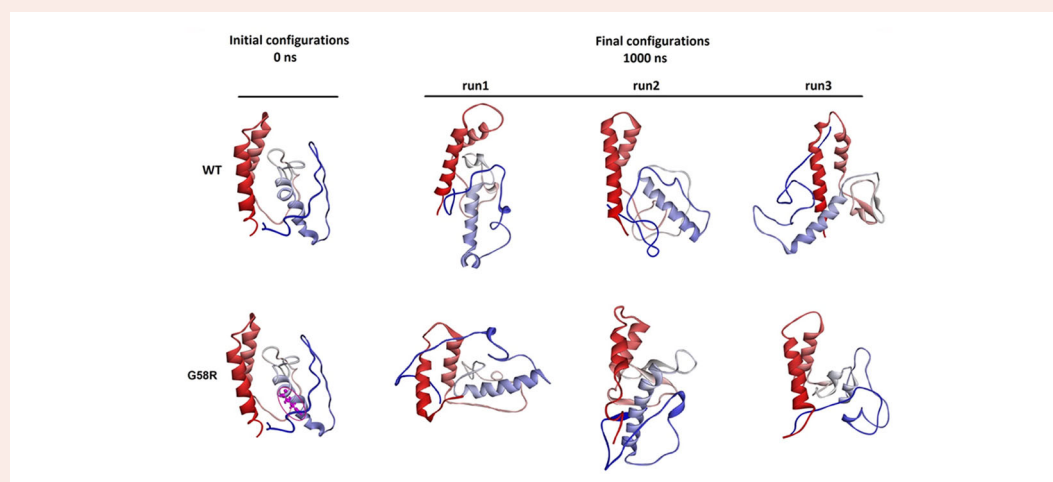
Abbreviations: CHCHD10: Coiled-coil-helix-coiled-coil-helix, 10, mitochondrial; WT: wild.type; MD: Molecular dynamics; PCA: Principal component analysis

CONTACT Hakan Alici ✉ hakanalici@beun.edu.tr 📧 Faculty of Sciences, Department of Physics, Zonguldak Bulent Ecevit University, Zonguldak, Turkey; Orkid Coskuner-Weber ✉ weber@tau.edu.tr 📧 Molecular Biotechnology, Turkish-German University, Istanbul, Turkey

🔓 Supplemental data for this article can be accessed online at https://doi.org/10.1080/07391102.2023.2227713.

1. Introduction

Mitochondrial myopathy is a genetic disorder that impacts the mitochondria, which are the powerhouses of the cell responsible for producing energy (Lim et al., 2023; Lu & Tarnopolsky, 2021; Vincent et al., 2016). The disease is caused by mutations in the genes which are responsible for producing the proteins and enzymes needed for proper mitochondrial function (Ahmed et al., 2018; El-Hattab & Scaglia, 2013). The symptoms of the disease can vary widely depending on the severity of the mutation and specific tissues affected by the mutation (DiMauro, 2006). Symptoms include exercise intolerance, muscle weakness, and fatigue (Beecher et al., 2022). Additional symptoms are difficulty in swallowing, respiratory problems, vision problems and hearing loss. There are several types of mitochondrial myopathy; Kearns-Sayre syndrome that typically presents with a combination of symptoms including heart block and retinitis pigmentosa (Tsang et al., 2018). An additional type poses symptoms such as lactic acidosis, stroke-like episodes, seizures, and dementia (Bhatti et al., 2017; He et al., 2020; Macdonald et al., 2018). High energy tissues, such as heart, brain and muscle tissue are usually impacted by mitochondrial disorders (Radelfahr & Klopstock, 2019). Mitochondrial disorders usually affect more than one organ in the human body. There are no effective treatments for mitochondrial myopathy, but treatment is prescribed for resolving or improving specific symptoms.

CHCHD10 is a gene that encodes the protein CHCHD10 (Burstein et al., 2018)Mutations in the CHCHD10 gene are associated with mitochondrial myopathy (Ajroud-Driss et al., 2015). Specifically, the CHCHD10 protein is involved in the regulation of mitochondrial function and plays a role in maintaining the structure of mitochondrial cristae (Z.-D. Zhou et al., 2017). Mitochondrial cristae can be defined as internal folds in the mitochondria that increase their surface area for energy production (Mannella, 2020). CHCHD10 gene mutations can disrupt the normal function of the CHCHD10 protein, leading to abnormal mitochondrial morphology, reduced mitochondrial respiration and impaired energy production (Xia et al., 2022). Mitochondrial stress triggers a response in mitochondria and nucleus and how these stress responses are coordinated are poorly understood. Recently, Shammas et al. characterized a family with myopathy caused by a dominant G58R mutation in the mitochondrial protein CHCHD10 (Shammas et al., 2022). For gaining insights into disease etiology, they developed a knockin (K1) mouse model and found that the mutant form of CHCHD10 aggregates in affected tissues, applying a toxic protein stress to the inner mitochondrial membrane. However, how G58R mutation impacts the structures of the wild-type CHCHD10 protein at the monomeric level in solution is unknown. The G58R mutation in CHCHD10 may alter the structure of the protein, impairing its ability to function properly in the mitochondria. As a result, individuals with the G58R mutation in CHCHD10 may experience mitochondrial myopathy.

The structure of the CHCHD10 protein contains a non-structured N-terminal region, a hydrophobic helix and a C-terminal CHCH domain which contains a Cx(9)C motif. CHCHD10 has intrinsically disordered protein regions (Alici

et al., 2022). Therefore, conventional experiments face challenges in the measurements of monomeric CHCHD10 structural ensembles in solution (Akbayrak et al., 2020). To the best of our knowledge, we presented recently the structural ensembles of CHCHD10 in an aqueous medium for the first time in the literature at the atomic level with dynamics (Alici et al., 2022). Moreover, we illustrated how S59L mutation of CHCHD10, which causes frontotemporal dementia-amyotrophic lateral sclerosis, impacts the structures of CHCHD10 in aqueous solution (Alici et al., 2022). It is known that the G58R mutation of CHCHD10 triggers mitochondrial myopathy (Shammas et al., 2022). However, the structural ensembles of CHCHD10^{WT} and CHCHD10^{G58R} remain to be compared with techniques that provide insights in aqueous solution at the atomic level with dynamics. The obtained knowledge about CHCHD10^{G58R} mutant structures in solution can be useful for designing more efficient treatments for mitochondrial myopathy. Furthermore, it is crucial to gain insights into the impacts of G58R mutation on CHCHD10^{WT} in solution regarding pathology, molecular biology and genetics, structural biology, and biochemistry. For understanding the structural ensemble properties of CHCHD10^{G58R} and how G58R mutation impact the structures of CHCHD10^{WT}, we link bioinformatics studies to homology modeling and multiple run molecular dynamics simulations of CHCHD10^{G58R} and CHCHD10^{WT}.

2. Methods

For consistency reasons, following our recent investigations (Alici et al., 2022), we conducted bioinformatics and homology modeling studies linked to multiple run molecular dynamics (MD) simulations on CHCHD10^{WT} and CHCHD10^{G58R} in an aqueous solution environment using the same protocols and methodologies. Specifically, we utilized the Iterative Threading ASSembly Refinement (I-TASSER) homology modeling approach (Yang & Zhang, 2015; Zheng et al., 2021; Zhou et al., 2022) for obtaining the initial CHCHD10^{WT} structure. The initial configuration of CHCHD10^{G58R} was produced by replacing the 58th glycine (G) residue with arginine (R). We set the temperature to 310 K using the Gromacs 5.1.4 software package (Berendsen et al., 1995) with a time step of 2 fs. The force field parameters (CHARMM36m for proteins and TIP3P for water) that we presented to yield excellent results for intrinsically disordered proteins in agreement with experiments were chosen (Alici et al., 2022; Huang et al., 2017). CHCHD10^{WT} and CHCHD10^{G58R} were solvated by 10,948 water molecules. Periodic boundary conditions were applied and the Particle Mesh Ewald method was used (Darden et al., 1993). A Cl$^-$ ion for CHCHD10^{WT} and two Cl$^-$ ions for CHCHD10^{G58R} were added for obtaining neutrality. The energies of CHCHD10^{WT} and CHCHD10^{G58R} were minimized using the steepest descent method and NVT as well as NPT ensembles were utilized for two-stage equilibrations of 2 ns, respectively (Allison et al., 2011). Each triple independent multiple run MD simulation was conducted for 1.0 μs for CHCHD10^{WT} and CHCHD10^{G58R} in separate runs, yielding a total simulation

time of 3.0 μs for each protein using varying velocity distributions (Alici et al., 2022). The Parrinello-Rahman barostat (Parrinello & Rahman, 1981) was used for keeping the pressure constant while Nose-Hover thermostat (Evans & Holian, 1985) was used for controlling temperature. The LINCS algorithm was applied (Hess, 2008). We used every 10 ps for saving the production run trajectories. The average free energy change surface area was calculated based on the radius of gyration and end-to-end distances using the following relationship:(Alici et al., 2022)

$$\Delta G = -k_B T[\ln P - \ln P_{max}]$$

where T is the temperature, k_B is the Boltzmann constant and P_{max} represents the maximum probability distribution. For calculating the intra-molecular hydrogen bonds, we used a cut-off distance of 3.5 Å and an angle cut-off of 130° between the acceptor and donor atoms (Alici et al., 2022). Using our recent studies, we defined a salt bridge using a cut-off distance of 7.0 Å for oppositely charged residues' centers of mass distance (Alici et al., 2022). Furthermore, intra-molecular interactions were determined using a distance between two residues centers of mass of 12.0 Å (Alici et al., 2022). Principal component analysis was determined for investigating the major motion dynamics in CHCHD10[WT] and CHCHD10[G58R] in solution. The first two principal components that were obtained from covariance matrix diagonalization of atomic coordinates were used in these calculations.

3. Results and discussion

Selected conformations from our multiple run molecular dynamics simulations including the initial structures (obtained from homology modeling) of CHCHD10[WT] and CHCHD10[G58R] are depicted in Figure 1. The average root mean square deviation (RMSD) values for CHCHD10[WT] and CHCHD10[G58R] are illustrated in Supporting Information section (Figure S7). The initial 200 ns of our simulation time are required for reaching convergency based on these results and this is in accord with our earlier studies (Alici et al., 2022). Therefore, we used the last 800 ns from each run (a total of 2.4 μs for each protein) in our analysis of CHCHD10[WT] and CHCHD10[G58R] in water, respectively. Figure 2 shows the average root mean square fluctuation (RMSF) for each amino acid residue for CHCHD10[WT] and CHCHD10[G58R] (Lim et al., 2022). Here, we note stark deviations in RMSF values in the N-terminal and mid-domain regions of CHCHD10 upon the mitochondrial myopathy-related G58R mutation.

3.1. Secondary structure properties

The residual average secondary structure elements along with their abundances for CHCHD10[WT] and CHCHD10[G58R] are depicted in Figure 3. Based on these findings, residues Ser39-Gly66, Cys102-Thr114, Leu119-Ser139 adopt prominent α-helical structures in the conformations of CHCHD10[G58R] while residues Gln41-Gly62, Cys102-Thr115, Leu119-Ser140 adopt abundant α-helical structures (probabilities higher than 10%) in the conformations of wild-type CHCHD10 in aqueous

solution. These findings indicate that residues His63-Gly66, which do not possess α-helix structure in the wild-type CHCHD10, adopt α-helical structure upon G58R mutation (> 10%). On the other hand Ser140 located in the C-terminus decreases its α-helix abundancy by 17% upon G58R mutation. Abundant β-sheet structure formation (with a probability higher than 10%) is detected at six residues of CHCHD10[WT]. Specifically, these residues are Ala21, Met65, Gly75, Gly76, Thr90, and Ala93. Regarding β-sheet structure formation in the conformations of CHCHD10[G58R], we detect abundant β-sheet formation at seven residues (Ala13, Met65, Ser74, Gly76, Val85, Gln86, and Met99). Even though the residues that adopt β-sheet structure differ from each other (except residues Met65 and Gly76) in these two proteins, indicating that their dynamics may be affected, the oligomerization may be affected by its location but not in its kinetics due to the similar number of residues adopting β-sheet structure with high probability. 3_{10}-helix formation (probability > 10%) is noted at Pro23-Ala25, Leu69 and Gln82-Ala84 in the structures of CHCHD10[G58R] while residues Pro23-Ala25, Gln82-Ala84 and Thr90-Ala92 adopt 3_{10}-helix structure in the conformations of CHCHD10[WT]. Prominent turn structure formation is detected at Pro2-Ala46, Ala60-Pro101, Ser113-Ser120, Tyr135-Ser140 in the structures of CHCHD10[G58R] and residues Pro2-Ala33, Ala37-Gln41, Met65-Pro96, Gly100, Pro101, Thr114-Leu119 adopt turn structure in the structures of CHCHD10[WT]. The β-sheet content is reduced in the structures of G58R mutant form in comparison to S59L mutant of CHCHD10 (especially in the N-terminal and mid-domain regions of CHCHD10) which we reported recently (Alici et al., 2022). Therefore, we expect a higher likelihood towards oligomerization and insolubility for mutant S59L CHCHD10 but not for the mutant G58R CHCHD10 protein in solution. This is consistent with observed insolubility and aggregation of the S59L mutant but normal solubility of the G58R mutant.

3.2. Free energy landscapes

Interestingly, the average end-to-end distance of CHCHD10[WT] ($R_{EE} = 12.86 \pm 3.23$ Å) becomes much longer upon G58R mutation ($R_{EE} = 20.36 \pm 3.51$ Å), indicating that the dynamics is different in CHCHD10[WT] and CHCHD10[G58R]. Specifically, this increase in end-to-end distance corresponds to 58%. On the other hand, the radius of gyration (R_g) is not significantly affected because the average R_g value for CHCHD10[WT] is 15.86 ± 021 Å and this value is 16.01 ± 0.27 Å for CHCHD10[G58R] in aqueous solution. To gain more insights into this behavior, we calculated the free energy landscapes of CHCHD10[WT] and CHCHD10[G58R] by means of R_g and R_{EE} values (Figure 4). The most preferred average R_g values range from 15.6 to 15.9 Å for CHCHD10[WT] and most preferred average R_g values range from 15.7 to 16.1 Å for CHCHD10[G58R], indicating that the thermodynamically preferred conformations possess similar compactness. Despite, the most preferred R_{EE} values range between 10.1 and 12.5 Å for CHCHD10[WT] while the most preferred R_{EE} values are in between 16.4 and 25.1 Å for CHCHD10[G58R] based on the free energy change surfaces. These results indicate that the
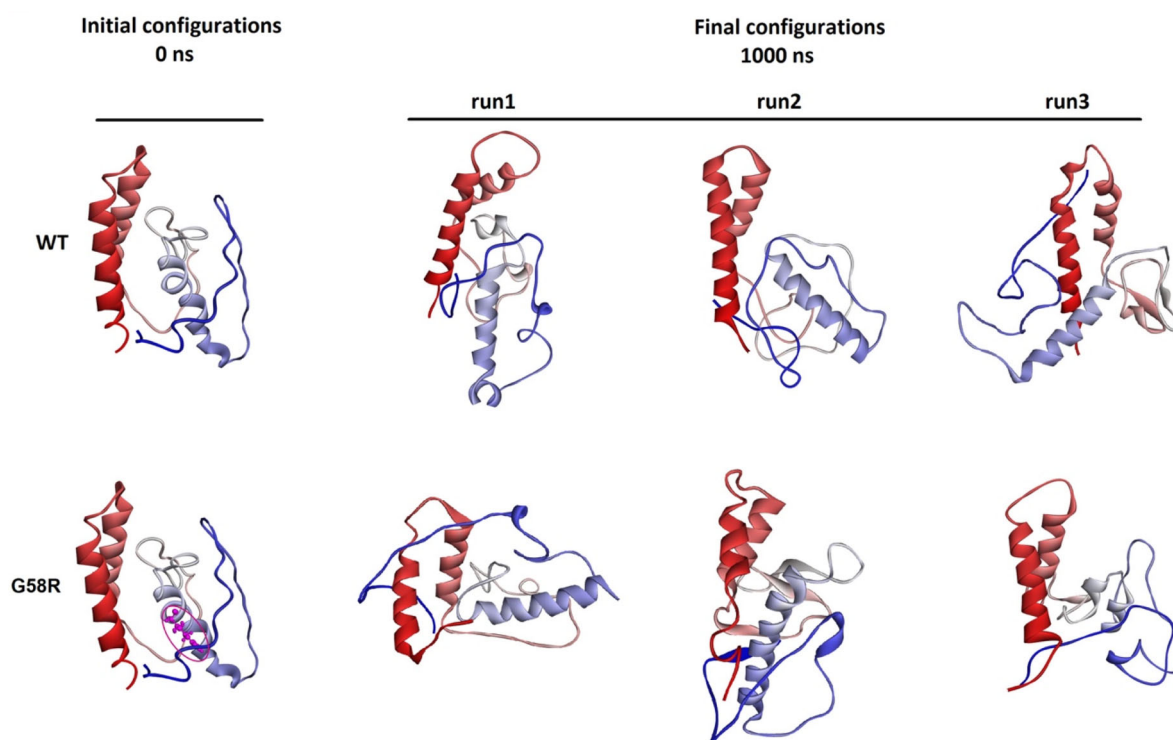
Figure 1. Representative conformations of CHCHD10^{WT} and CHCHD10^{G58R} from our multiple run MD simulations.
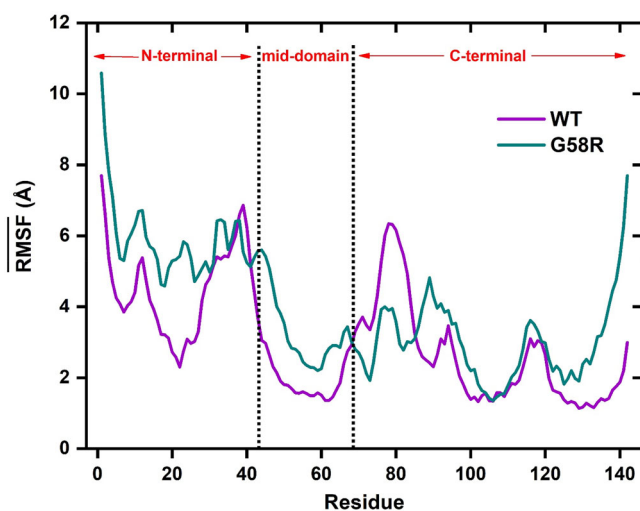

Figure 2. The average RMSF values for CHCHD10^{WT} and CHCHD10^{G58R}.

compactness is not but the dynamics is significantly altered upon G58R mutation of CHCHD10 in water.

To gain insight into these dynamical effects, we calculated the Ramachandran plots for CHCHD10^{WT} and CHCHD10^{G58R} and results are depicted in Figure 5. We also calculated the impacts of G58R mutation on neighboring residues *via* Ramachandran plots (Supplementary Information Section). We see stark differences in the densities between $\Phi = -45$ and $100°$ and $\Psi = 40$ and -110. We also observe significant differences in the densities between $\Phi = 45$ and $90°$ and $\Psi = -135$ and $-180°$. It is noted that the CHCHD10^{WT} is more flexible than CHCHD10^{G58R} and that the guanidine group of arginine is providing a steric hindrance in the dynamics of the chain. We note a significant effect of G58R mutation on far and near neighboring residues (see Supplementary Information

section). Examining the 58th amino acid position for CHCHD10WT and CHCHD10G58R, it is observed that the conformations are clustered on a single dominant region covering the α-helix and turn areas. Evaluating the neighbor amino acids (45–57 amino acid regions), the dihedral angle regions of Val55, Ala56, Val57 residues of both CHCHD10WT and CHCHD10G58R proteins have an almost complete conformational overlap. Also, it is detected for the amino acid positions (except for Gly54) between Met45 and Gly54 that CHCHD10WT protein has a single dominant conformational cluster found mostly in the α-helix and turn areas while CHCHD10G58R protein has at least two dominant conformational clusters located in α-helix, turn areas and the other in the β-sheet areas. When the neighbor amino acids (59–68 amino acid region in mid domain) at positions after mutation residue 58 are examined, it is seen that for Ser59, CHCHD10WT and CHCHD10G58R proteins show a single dominant angular cluster located in mostly in the α-helix. On the other hand, for Val60 and Val61 residues, conformations of CHCHD10WT are clustered on a single dominant region covering the α-helix and turn areas while CHCHD10G58R protein has two different dominant conformations, which one of them is observed to overlap with CHCHD10WT whereas the other is located in the β-sheet areas. Also, results for Gly62-Ala68 amino acid regions indicate that angular distributions of both CHCHD10WT and CHCHD10G58R proteins are scattered at least two dominant region and thus the point mutation has a stark effect on amino acid conformations in this region. The formed hydrogen bond numbers in CHCHD10^{WT} and CHCHD10^{G58R} do not present a stark deviation from each other (Figure 6), indicating that the G58R mutation—that is affecting the dynamics (see above)—is not impacting the formed hydrogen bond numbers significantly. Also, we carried out independent samples *t*-test
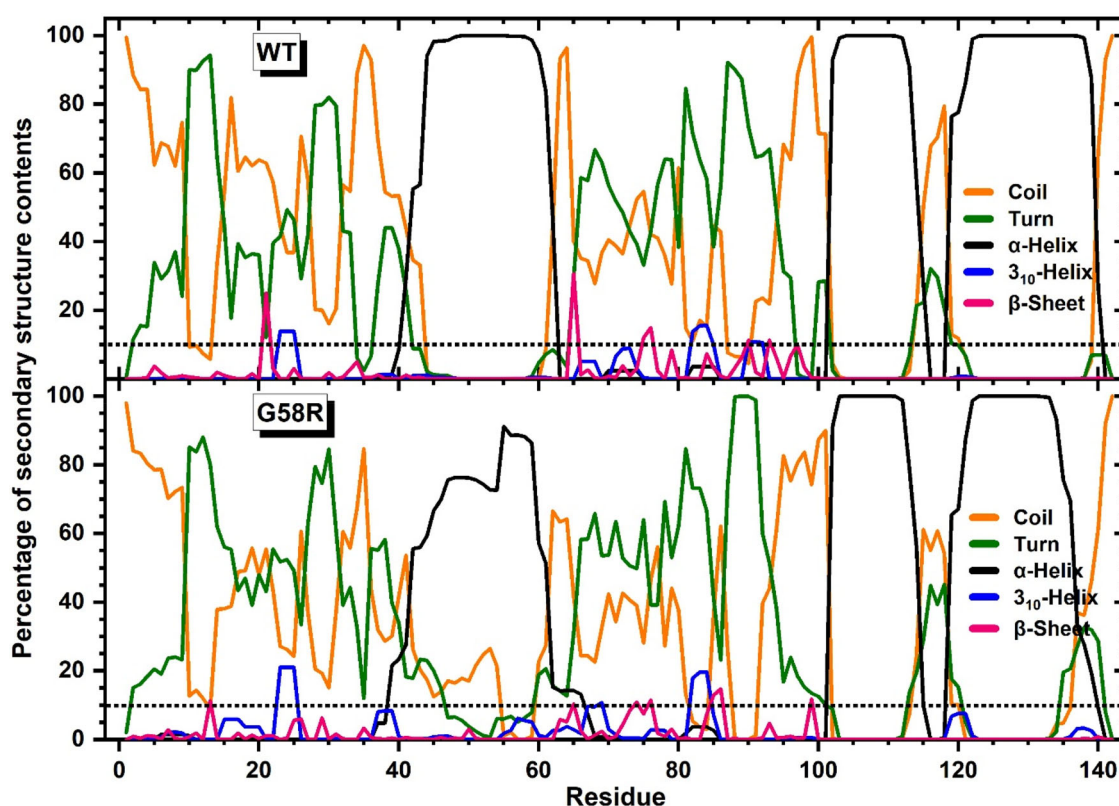
Figure 3. The average secondary structure element abundances per amino acid for CHCHD10^WT and CHCHD10^G58R in water. Coil (brown), turn (green), α-helix (black), 310-helix (blue) and β-sheet (pink).
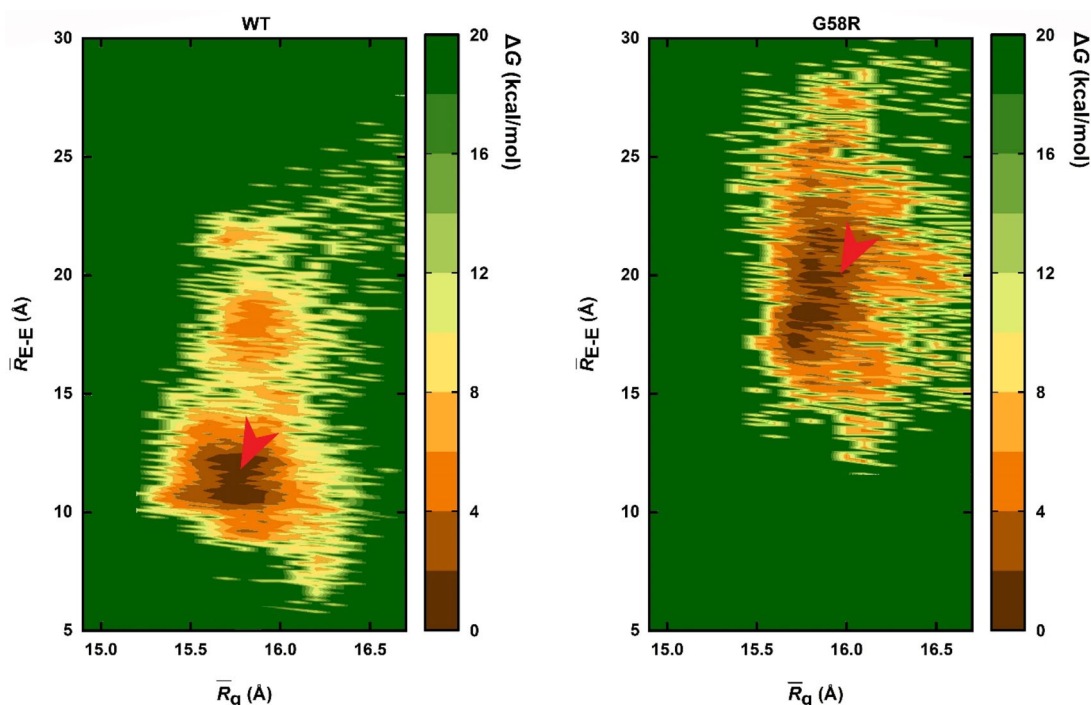

Figure 4. Free energy surface areas of wild- and G58R mutant-type CHCHD10 based on average R_g and R_{EE} values.

analyses for the formed hydrogen bond numbers in CHCHD10WT and CHCHD10G58R and p values were found to be 0, which indicates that there are significant differences in the results. According to this findings, it is inferred that the G58R mutation both affect the dynamics (see above) and impact the formed hydrogen bond numbers significantly.

3.3. Tertiary structure properties

The tertiary structure properties based on intramolecular contact maps show a large deviation from each other upon G58R mutation in aqueous solution. Namely, the interactions within the N-terminal are more prominent in the structural
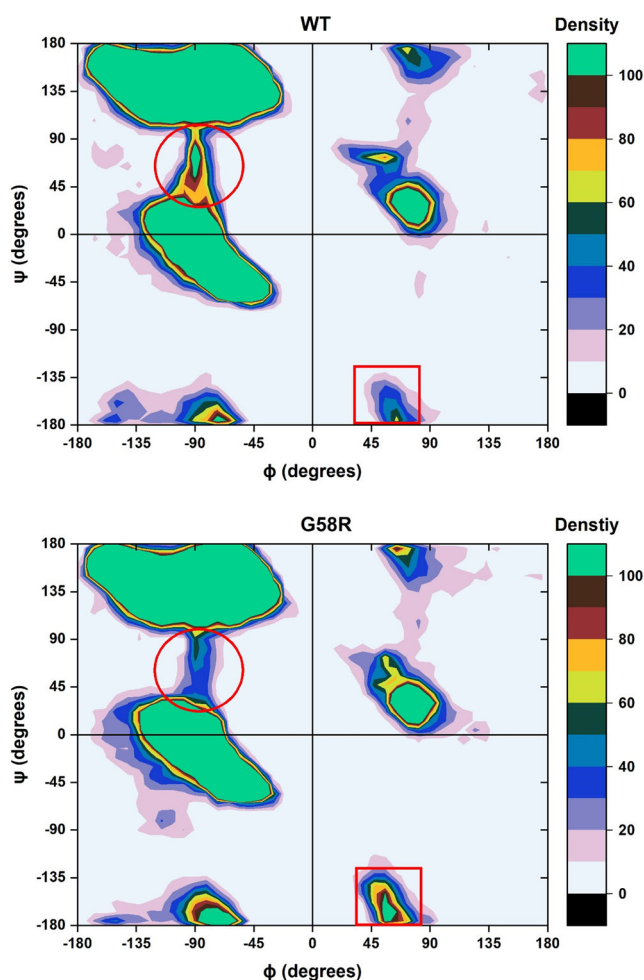
Figure 5. Ramachandran density plots demonstrating the specific torsional angles for wild- and G58R mutant-type CHCHD10.
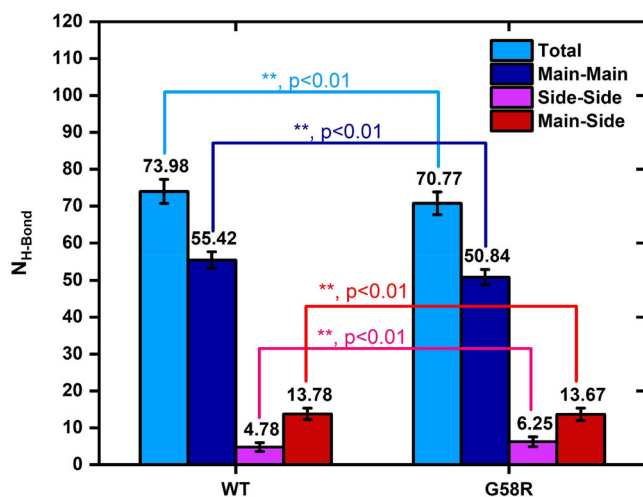

Figure 6. The average hydrogen bond numbers formed in wild- and G58R mutant-type CHCHD10.

Figure 7. The intramolecular interaction maps of wild- and G58R mutant-type CHCHD10.

ensembles of CHCHD10^{G58R} in comparison to CHCHD10^{WT} while more abundant interactions are detected for the N-terminal and mid-domain or C-terminal regions in the structural ensembles of CHCHD10^{WT}. Furthermore, a larger number of residues locat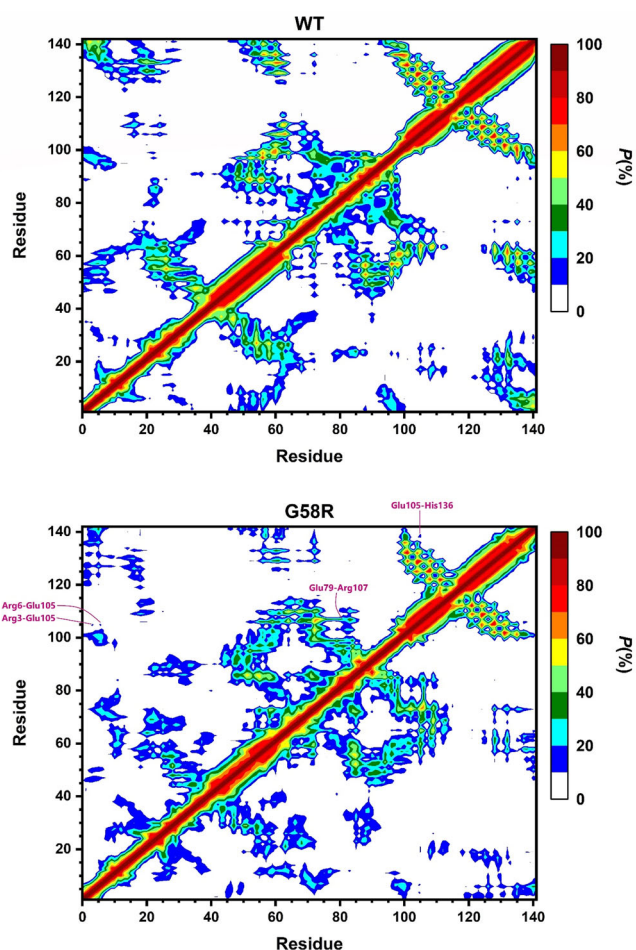ed in the mid-domain regions interact with each other upon G58R mutation of CHCHD10. Moreover, less abundant interactions are detected between the mid-domain and C-terminal regions upon G58R mutation. Interestingly, a similar trend is also obtained for interactions within the C-terminal region upon G58R mutation (Figure 7). These differences in tertiary structure properties may cause different dynamics trends for the two IDPRs in solution. We also note that the G58R mutation causes the formation of additional salt bridges between Arg3 and Glu105, Arg6 and Glu105, Arg107 and Glu79, and His136 and Glu105 in comparison to CHCHD10^{WT} in water (Table 1).

3.4. Principal component analysis

For gaining insights onto the conformational dynamics in the structural ensembles of CHCHD10^{WT} and CHCHD10^{G58R}, we calculated the trends using principal component analysis (PCA) depending on the first two average principal coordinates and the conformational free energy was identified as an additional coordinate. Figure 8 presents our PCA results. We notice—based on the calculated first and seconds principal components—that the dynamics differs between these two proteins because the CHCHD10^{G58R} protein occupies more subspace with favorable free energy values in comparison to its wild-type form. All in all, based on these findings,

Table 1. The formed average salt bridge distances including their statistical deviations between specific amino acid residues of wild- and G58R mutant-type CHCHD10.

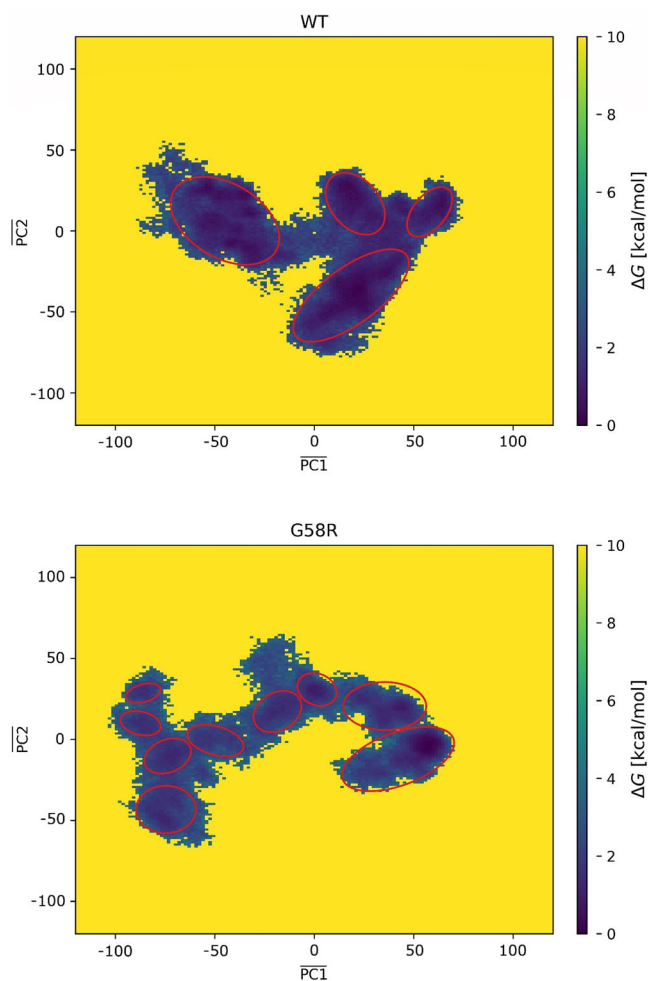| Residue	Residue	CHCHD10^{WT} (Å)	CHCHD10^{G58R} (Å)
Asp111	Arg107	6.48 (1.62)	5.34 (1.46)
Glu79	Arg107	–	12.41 (1.85)
Glu105	Arg3	–	16.22 (4.64)
Glu105	Arg6	–	17.33 (3.32)
Glu105	His136	–	10.03 (0.65)
Glu123	Lys130	8.69 (0.88)	9.98 (0.92)
Glu127	Lys130	4.34 (1.07)	6.30 (1.46)

Figure 8. (A) Free energy surface areas of wild-type and G58R mutant-type CHCHD10 from our PCA analysis.

we can conclude that the mitochondrial myopathy-related G58R mutation increases the flexibility in the dynamics of the CHCHD10 in solution.

These observations are also in line with the evaluation of the effect of the G58R mutation on local intrinsic disorder predisposition of the human CHCHD10. This is illustrated by Figure 9, which represents intrinsic disorder profiles computed for the wild type of CHCHD10 (Figure 9A) and for the G58R mutant (Figure 9B), whereas Figure 9C shows "difference disorder spectra", where the profiles of the wild-type CHCHD10 generated by a set commonly used predictors, PONDR® VLXT, PONDR® VL3, PONDR® VSL2, PONDR® FIT, IUPred short, and IUPred long (Dosztányi et al., 2005; Erdős & Dosztányi, 2020; Mészáros et al., 2018; Xue et al.,

2010) were subtracted from the corresponding disorder profiles calculated for the G58R mutant CHCHD10 by the same predictors. Since different disorder predictors use different definitions of intrinsic disorder and different sequence attributes (see Table 2 for the brief description of tools utilized in this study), the accepted practice in the field is to use several different predictors that might generate some complementary information. This analysis revealed that the G58R mutation causes some decrease in the local intrinsic disorder predisposition of the N-terminal region (residues 1–102, which are characterized by the mean disorder scores exceeding the threshold of 0.5), as its mean disorder score slightly decreases from 0.824 ± 0.117 to 0.818 ± 0.125. The effect of the mutation is more obvious if its close vicinity is considered. In fact, for the region comprising residues 50–75, the mean disorder score decreases from 0.695 ± 0.059 to 0.674 ± 0.068 (cf. Figure 9A, B). To get better representation of this effect on local disorder predisposition of human CHCHD10 protein, we looked at the "difference disorder spectra" Figure 9C that zooms into the region spanning residues Gly40-Val85 and that were obtained subtracting disorder profile generated for the wild-type CHCHD10 by a given predictor from the corresponding disorder profile of the G58R mutant generated by the same predictor. In the corresponding plot, the negative values of the resulting differences indicate that the local disorder propensity of CHCHD10 is decreased due to the G58R mutation, whereas positive values indicate the mutation-induced increase in the local disorder propensity. Figure 9C also shows that different predictors "feel" the effect of this mutation rather differently, where IUPred_Long and especially IUPred_short indicate that the local intrinsic disorder propensity is somewhat increased in the vicinity of the G58R mutation. On the other hand, PONDR® VLXT, which is known for its high sensitivity to local sequence peculiarities, suggest rather substantial drop in the local disorder propensity (for the aforementioned 50–75 region, the mean disorder score decreases from 0.78 ± 0.18 to 0.68 ± 0.23). Furthermore, since the G58R mutation is located in the middle of the disorder-based binding site (residues 38–74) predicted by ANCHOR, one can expect some changes in the interactivity of the CHCHD10 caused by the G58R mutation (Dosztányi et al., 2009). These dynamic differences may be associated with the soluble but punctate aggregates of the G58R protein observed in the CHCHD10^{G58R} knock-in mouse model of mitochondrial myopathy (Shammas et al., 2022).

4. Conclusions

We reported the structures of G58R mutant CHCHD10 and the impacts of G58R mutation on the wild-type CHCHD10 structures in an aqueous solution environment. Our findings show that the secondary structural properties, tertiary structural properties, free energy landscapes, Ramachandran plots, end-to-end distance, principal component analysis results are impacted by the G58R mutation of CHCHD10 at the monomeric level in an aqueous solution medium. The radius of gyration values are similar for wild-type CHCHD10 and G58
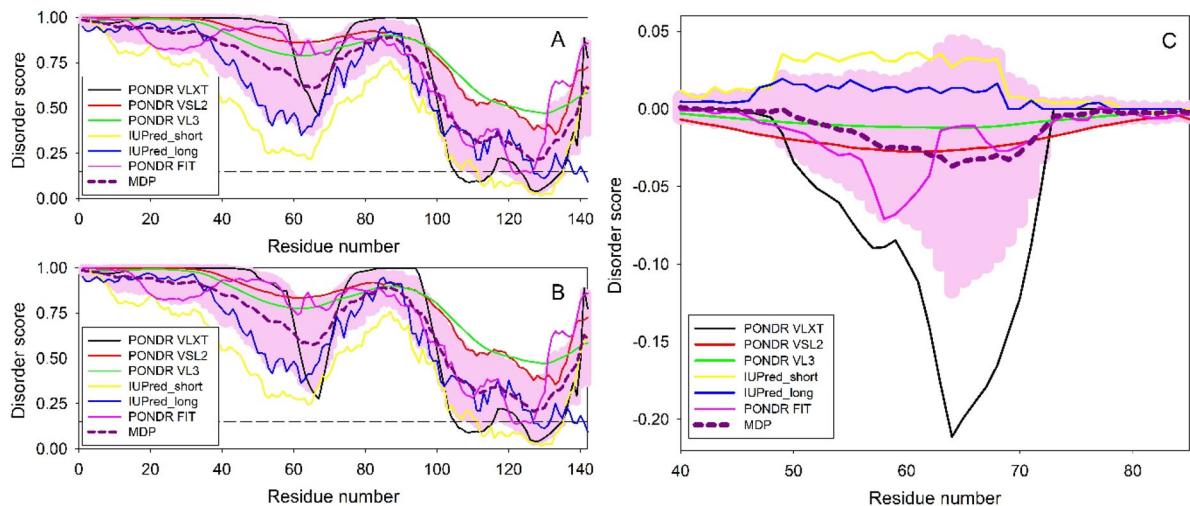
Figure 9. Impact of the G58R genetic mutation on intrinsic disorder predisposition of CHCHD10 (UniProt ID: Q8WYQ3). (A) Intrinsic disorder profile computed for wild type of CHCHD10 by a set of disorder predictors. (B) Intrinsic disorder profile of the G58R mutant form calculated by the same predictors. (C) Visualization of the impact of the G58R mutation on local disorder propensity as "disorder spectra deviation", which were computed by subtracting the profile of wild-type CHCHD10 generated by PONDR® VLXT, PONDR® VSL2, PONDR® VL3, IUPred2A long, IUPred 2 A short and PONDR® FIT, from the analogous disorder profiles calculated for the G58R mutant-type CHCHD10. Average disorder profile along with standard deviations are presented as dashed bold dark pink line and light pink shade.

Table 2. Brief description of disorder predictors used in this study.

Predictor name	Brief description	Reference
PONDR® VLXT	The merger of three predictors, one trained on **V**ariously characterized **L**ong disordered regions and two trained on **X**-ray characterized **T**erminal disordered regions; very sensitive to local disorder peculiarities; useful for predicting molecular recognition features, MoRFs, short regions of disorder capable of undergoing disorder-to-order transition at interaction with specific partners.	Romero et al. (2001)
PONDR® VL3	A feed-forward neural network that was trained on long regions of disorder that were characterized by various methods; better for proteins that contain high disorder content or long disordered regions.	Peng et al. (2006)
PONDR® VLS2	Combines two predictors optimized for long (>30 residues) and short (≤30 residues) disordered regions, respectively, using weights generated by a third meta-predictor; statistically better for proteins containing both structure and disorder; one of the best stand-alone per-residue disorder predictors.	Peng et al. (2005)
IUPred2_ShortIUPred2_Long	Based on the statistical inter-residue interaction potentials approximated from the solved protein structures; trained on a reference set of non-redundant globular proteins; can be used for prediction of short and long intrinsically disordered regions of proteins based on the estimated energy content;	Mészáros et al. (2018)
PONDR® FIT	A metapredictor that uses outputs of PONDR® VLXT, PONDR® VL3, PONDR® VSL2, PONDR® FIT and IUPred as input; statistically not different from PONDR® VL3 for fully disordered and fully structured proteins, and slightly better (1 std) than PONDR® VSL2, when both structure and disorder are present	Xue et al. (2010)

mutant CHCHD10 at the monomeric level in water, indicating that the compactness of the protein is not significantly affected by the genetic mutation. We also show that the G58R mutation causes some decrease in the local intrinsic disorder predisposition of the N-terminal region of CHCHD10 with different predictors "feeling" the effect of this mutation rather differently. Furthermore, since the G58R mutation is located in the middle of the disorder-based binding site (residues 38–74), it is likely that the G58R mutation can trigger some changes in the interactivity of the CHCHD10. These structural changes may also impact the oligomerization of CHCHD10 upon G58R genetic mutation. Such dynamic structural differences may also impact CHCHD10 interactions with other proteins in mitochondria, leading to mitochondrial myopathy.

All in all, our data show that the structural ensemble properties and dynamics of CHCHD10^G58R, which is at the center of mitochondrial myopathy, differ from those of wild-type CHCHD10. These results may be useful for designing an efficient treatment for mitochondrial myopathy.

Disclosure statement

Funding

ORCID

Vladimir N. Uversky http://orcid.org/0000-0002-4037-5857

References

Ahmed, S. T., Craven, L., Russell, O. M., Turnbull, D. M., & Vincent, A. E. (2018). Diagnosis and treatment of mitochondrial myopathies. *Neurotherapeutics : The Journal of the American Society for Experimental NeuroTherapeutics*, 15(4), 943–953. https://doi.org/10.1007/s13311-018-00674-4

Ajroud-Driss, S., Fecto, F., Ajroud, K., Lalani, I., Calvo, S. E., Mootha, V. K., Deng, H.-X., Siddique, N., Tahmoush, A. J., Heiman-Patterson, T. D., & Siddique, T. (2015). Mutation in the novel nuclear-encoded mitochondrial protein CHCHD10 in a family with autosomal dominant mitochondrial myopathy. *Neurogenetics*, 16(1), 1–9. https://doi.org/10.1007/s10048-014-0421-1

Akbayrak, I. Y., Caglayan, S. I., Ozcan, Z., Uversky, V. N., & Coskuner-Weber, O. (2020). Current challenges and limitations in the studies of intrinsically disordered proteins in neurodegenerative diseases by computer simulations. *Current Alzheimer Research*, 17(9), 805–818. https://doi.org/10.2174/1567205017666201109094908

Alici, H., Uversky, V. N., Kang, D. E., Woo, J. A., & Coskuner-Weber, O. (2022). Structures of the wild-type and S59L mutant CHCHD10 proteins important in amyotrophic lateral sclerosis-frontotemporal dementia. *ACS Chemical Neuroscience*, 13(8), 1273–1280. https://doi.org/10.1021/acschemneuro.2c00011

Allison, T. C., Coskuner, O., & Gonzalez, C. A. (Eds.). (2011). *Metallic systems: A quantum chemist's perspective*. CRC Press. https://doi.org/10.1201/b10835

Beecher, G., Fleming, M. D., & Liewluck, T. (2022). Hereditary myopathies associated with hematological abnormalities. *Muscle & Nerve*, 65(4), 374–390. https://doi.org/10.1002/mus.27474

Berendsen, H. J. C., van der Spoel, D., & van Drunen, R. (1995). GROMACS: A message-passing parallel molecular dynamics implementation. *Computer Physics Communications*, 91(1-3), 43–56. https://doi.org/10.1016/0010-4655(95)00042-E

Bhatti, J. S., Bhatti, G. K., & Reddy, P. H. (2017). Mitochondrial dysfunction and oxidative stress in metabolic disorders—A step towards mitochondria based therapeutic strategies. *Biochimica et Biophysica Acta. Molecular Basis of Disease*, 1863(5), 1066–1077. https://doi.org/10.1016/j.bbadis.2016.11.010

Burstein, S. R., Valsecchi, F., Kawamata, H., Bourens, M., Zeng, R., Zuberi, A., Milner, T. A., Cloonan, S. M., Lutz, C., Barrientos, A., & Manfredi, G. (2018). In vitro and in vivo studies of the ALS-FTLD protein CHCHD10 reveal novel mitochondrial topology and protein interactions. *Human Molecular Genetics*, 27(1), 160–177. https://doi.org/10.1093/hmg/ddx397

Darden, T., York, D., & Pedersen, L. (1993). Particle mesh Ewald: An *N* log (*N*) method for Ewald sums in large systems. *The Journal of Chemical Physics*, 98(12), 10089–10092. https://doi.org/10.1063/1.464397

DiMauro, S. (2006). Mitochondrial myopathies. *Current Opinion in Rheumatology*, 18(6), 636–641. https://doi.org/10.1097/01.bor.0000245729.17759.f2

Dosztányi, Z., Csizmok, V., Tompa, P., & Simon, I. (2005). IUPred: Web server for the prediction of intrinsically unstructured regions of proteins based on estimated energy content. *Bioinformatics (Oxford, England)*, 21(16), 3433–3434. https://doi.org/10.1093/bioinformatics/bti541

Dosztányi, Z., Mészáros, B., & Simon, I. (2009). ANCHOR: Web server for predicting protein binding regions in disordered proteins. *Bioinformatics (Oxford, England)*, 25(20), 2745–2746. https://doi.org/10.1093/bioinformatics/btp518

El-Hattab, A. W., & Scaglia, F. (2013). Mitochondrial DNA depletion syndromes: Review and updates of genetic basis, manifestations, and therapeutic options. *Neurotherapeutics : The Journal of the American Society for Experimental NeuroTherapeutics*, 10(2), 186–198. https://doi.org/10.1007/s13311-013-0177-6

Erdős, G., & Dosztányi, Z. (2020). Analyzing protein disorder with IUPred2A. *Current Protocols in Bioinformatics*, 70(1), e99. https://doi.org/10.1002/cpbi.99

Evans, D. J., & Holian, B. L. (1985). The Nose–Hoover thermostat. *The Journal of Chemical Physics*, 83(8), 4069–4074. https://doi.org/10.1063/1.449071

He, Z., Ning, N., Zhou, Q., Khoshnam, S. E., & Farzaneh, M. (2020). Mitochondria as a therapeutic target for ischemic stroke. *Free Radical Biology & Medicine*, 146, 45–58. https://doi.org/10.1016/j.freeradbiomed.2019.11.005

Hess, B. (2008). P-LINCS: A parallel linear constraint solver for molecular simulation. *Journal of Chemical Theory and Computation*, 4(1), 116–122. https://doi.org/10.1021/ct700200b

Huang, J., Rauscher, S., Nawrocki, G., Ran, T., Feig, M., de Groot, B. L., Grubmüller, H., & MacKerell, A. D. (2017). CHARMM36m: An improved force field for folded and intrinsically disordered proteins. *Nature Methods*, 14(1), 71–73. https://doi.org/10.1038/nmeth.4067

Lim, Y. Y., Miskon, A., & Zaidi, A. M. A. (2022). Structural strength analyses for low brass filler biomaterial with anti-trauma effects in articular cartilage scaffold design. *Materials*, 15(13), 4446. https://doi.org/10.3390/ma15134446

Lim, Y. Y., Zaidi, A. M. A., & Miskon, A. (2023). Combining copper and zinc into a biosensor for anti-chemoresistance and achieving osteosarcoma therapeutic efficacy. *Molecules*, 28(7), 2920. https://doi.org/10.3390/molecules28072920

Lu, J.-Q., & Tarnopolsky, M. A. (2021). Mitochondrial neuropathy and neurogenic features in mitochondrial myopathy. *Mitochondrion*, 56, 52–61. https://doi.org/10.1016/j.mito.2020.11.005

Macdonald, R., Barnes, K., Hastings, C., & Mortiboys, H. (2018). Mitochondrial abnormalities in Parkinson's disease and Alzheimer's disease: Can mitochondria be targeted therapeutically? *Biochemical Society Transactions*, 46(4), 891–909. https://doi.org/10.1042/BST20170501

Mannella, C. A. (2020). Consequences of folding the mitochondrial inner membrane. *Frontiers in Physiology*, 11, 536. https://doi.org/10.3389/fphys.2020.00536

Mészáros, B., Erdos, G., & Dosztányi, Z. (2018). IUPred2A: Context-dependent prediction of protein disorder as a function of redox state and protein binding. *Nucleic Acids Research*, 46(W1), W329–W337. https://doi.org/10.1093/nar/gky384

Parrinello, M., & Rahman, A. (1981). Polymorphic transitions in single crystals: A new molecular dynamics method. *Journal of Applied Physics*, 52(12), 7182–7190. https://doi.org/10.1063/1.328693

Peng, K., Radivojac, P., Vucetic, S., Dunker, A. K., & Obradovic, Z. (2006). Length-dependent prediction of protein intrinsic disorder. *BMC Bioinformatics*, 7(1), 208. https://doi.org/10.1186/1471-2105-7-208

Peng, K., Vucetic, S., Radivojac, P., Brown, C. J., Dunker, A. K., & Obradovic, Z. (2005). Optimizing long intrinsic disorder predictors with protein evolutionary information. *Journal of Bioinformatics and Computational Biology*, 3(1), 35–60. https://doi.org/10.1142/s0219720005000886

Radelfahr, F., & Klopstock, T. (2019). [Mitochondrial diseases]. *Der Nervenarzt*, 90(2), 121–130. https://doi.org/10.1007/s00115-018-0666-2

Romero, P., Obradovic, Z., Li, X., Garner, E. C., Brown, C. J., & Dunker, A. K. (2001). Sequence complexity of disordered protein. *Proteins: Structure, Function, and Genetics*, 42(1), 38–48. https://doi.org/10.1002/1097-0134(20010101)42:1<38::aid-prot50>3.0.co;2-3

Shammas, M. K., Huang, X., Wu, B. P., Fessler, E., Song, I. Y., Randolph, N. P., Li, Y., Bleck, C. K., Springer, D. A., Fratter, C., Barbosa, I. A., Powers, A. F., Quirós, P. M., Lopez-Otin, C., Jae, L. T., Poulton, J., & Narendra, D. P. (2022). OMA1 mediates local and global stress responses against protein misfolding in CHCHD10 mitochondrial myopathy. *Journal of Clinical Investigation*, 132(14), e157504. https://doi.org/10.1172/JCI157504

Tsang, S. H., Aycinena, A. R. P., & Sharma, T. (2018). Mitochondrial disorder: Kearns-Sayre Syndrome. *Advances in Experimental Medicine and Biology*, 1085, 161–162. https://doi.org/10.1007/978-3-319-95046-4_30

Vincent, A. E., Ng, Y. S., White, K., Davey, T., Mannella, C., Falkous, G., Feeney, C., Schaefer, A. M., McFarland, R., Gorman, G. S., Taylor, R. W., Turnbull, D. M., & Picard, M. (2016). The spectrum of mitochondrial

ultrastructural defects in mitochondrial myopathy. *Scientific Reports*, *6*, 30610. https://doi.org/10.1038/srep30610

Xia, W., Qiu, J., Peng, Y., Snyder, M. M., Gu, L., Huang, K., Luo, N., Yue, F., & Kuang, S. (2022). Chchd10 is dispensable for myogenesis but critical for adipose browning. *Cell Regeneration*, *11*(1), 14. https://doi.org/10.1186/s13619-022-00111-0

Xue, B., Dunbrack, R. L., Williams, R. W., Dunker, A. K., & Uversky, V. N. (2010). PONDR-FIT: A meta-predictor of intrinsically disordered amino acids. *Biochimica et Biophysica Acta*, *1804*(4), 996–1010. https://doi.org/10.1016/j.bbapap.2010.01.011

Yang, J., & Zhang, Y. (2015). I-TASSER server: New development for protein structure and function predictions. *Nucleic Acids Research*, *43*(W1), W174–W181. https://doi.org/10.1093/nar/gkv342

Zheng, W., Zhang, C., Li, Y., Pearce, R., Bell, E. W., & Zhang, Y. (2021). Folding non-homologous proteins by coupling deep-learning contact maps with I-TASSER assembly simulations. *Cell Reports Methods*, *1*(3), 100014. https://doi.org/10.1016/j.crmeth.2021.100014

Zhou, Z.-D., Saw, W.-T., & Tan, E.-K. (2017). Mitochondrial CHCHD-containing proteins: Physiologic functions and link with neurodegenerative diseases. *Molecular Neurobiology*, *54*(7), 5534–5546. https://doi.org/10.1007/s12035-016-0099-5

Zhou, X., Zheng, W., Li, Y., Pearce, R., Zhang, C., Bell, E. W., Zhang, G., & Zhang, Y. (2022). I-TASSER-MTD: A deep-learning-based platform for multi-domain protein structure and function prediction. *Nature Protocols*, *17*(10), 2326–2353. https://doi.org/10.1038/s41596-022-00728-0